Wind and Wave Measurements Using Complex ERS-2 SAR Wave Mode Data

Susanne Lehner, Johannes Schulz-Stellenfleth, Birgit Schättler, Helko Breit, and Jochen Horstmann

***Abstract*—A global dataset of complex synthetic aperture (SAR) images is processed from wave mode raw data acquired by the ERS-2 satellite. Using these data, different algorithms for wind and wave measurements recently developed in view of future ENVISAT ASAR data are analyzed on a statistical basis.**

Different aspects of complex SAR wave mode processing with the DLR processor BSAR are discussed and global statistics of processing parameters are presented.

Single-look complex (SLC) imagettes give the opportunity to apply multilook techniques in range as well as in azimuth. Such methods are used to reduce speckle noise or to analyze the time evolution of the ocean surface cross section during SAR integration time. A global analysis of different new algorithms for wind and ocean wave measurements, taking advantage of SLC data, is given. Wind speed is estimated with the azimuthal cross-correlation algorithm (CCA). As a modification of the existing CCA, range multilooking is used to deal with the speckle bias. Homogeneity of the imagettes is considered. Wind speed is derived from mean SAR image intensities taking into account wind direction (CMOD algorithm). Comparison with collocated ERS-2 scatterometer data shows reasonable agreement with the CCA and good agreement for the CMOD approach.

Using imagettes instead of image power spectra allows us to study ocean surface features caused by natural slicks, sea ice, or atmospheric processes. The impact of these phenomena on SCAT measurements is considered.

Cross spectral methods are used to derive the ocean wave propagation direction from complex imagettes on a global basis. Comparison with model data provided by the European Center for Medium Range Weather Forecast (ECMWF), Reading, U.K., shows good agreement.

***Index Terms*—ERS wave mode, ocean waves, SAR, wind speed estimation.**

I. Introduction

SINCE the launch of the ERS-1 and ERS-2 satellites in 1991 and 1995, synthetic aperture radar (SAR) images have been acquired over the oceans on a continuous basis. Full swath scenes of 100×100 km size are taken where receiving stations are in line of sight (image mode), whereas 6×10 km images (imagettes) are acquired every 200 km along the orbit (wave mode). Due to their all-weather capability and high resolution, SAR systems have become a valuable measurement tool for wind speed and ocean waves [1]–[3].

Manuscript received September 22, 1999; revised April 7, 2000. The study was supported by the German Ministry of Education, Science, and Technology (BMBF) in the framework of the ENVOC project.

S. Lehner, J. Schulz-Stellenfleth, B.Schättler, and H. Breit are with the Institute of Remote Sensing Technology, German Aerospace Center (DLR), Oberpfaffenhofen, Germany.

J. Horstmann is with the GKSS Research Center, Geesthacht, Germany.

Publisher Item Identifier S 0196-2892(00)08906-3.

It is clear that SAR imaging of the sea surface is a complex mechanism influenced by many different processes, e.g., wind, currents, slicks, or rain. However, the basic imaging mechanisms are well understood by now [2]–[7].

Quite a few studies were published about the use of ERS wave mode data for wind and wave measurements. These are mostly concerned with the analysis of user wave (UWA) spectra, which are the standard European Space Agency (ESA), Noordwijk, The Netherlands, product [1], [8]–[10]. UWA spectra are coarsely gridded image power spectra derived from imagettes with a directional resolution of 15° and 10 wavenumber bins logarithmically spaced between 66–660 m (recently changed from 100 m to 1000 m) [11]. The complex imagettes themselves are so far not available from ESA as a standard product. An analysis of imagette intensities has been performed by Kerbaol [12].

Recently, new algorithms were developed to derive wind speed and ocean wave spectra from complex SAR images [13], making use of the additional phase information contained in these data. Up to now, these algorithms were only tested using image mode data [14], which are not suited for global statistical analysis, as they can be acquired over the open ocean only when in line of sight of an antenna station.

This paper aims at testing and improving different SAR wind and wave measurement methods using a global complex ERS-2 SAR wave mode dataset. The study is a preparation for the new data products available from the ASAR (advanced SAR) of the ENVISAT satellite to be launched in the year 2001. As ENVISAT will not carry a scatterometer (SCAT), the development of ASAR wind measurement techniques is of special interest. As the ERS SAR, the ASAR will operate at C-band and collect data in image mode and wave mode. The ENVISAT ASAR wave mode will have some advanced features, as shown in Table I.

To prepare for ENVISAT data, ERS-2 wave mode raw data were processed to single-look complex imagettes using the BSAR processor developed at the German Remote Sensing Data Center (DFD), Oberpfaffenhofen, Germany. An example of an imagette quicklook from this dataset showing ocean waves is given in Fig. 1.

In this study, three main points are investigated.

1) It is demonstrated how complex imagettes can be used to derive additional information on wind speed, sea state, and surface features as compared to UWA spectra.
2) As wave mode is available at the same time and location within the larger SCAT pixels (50×50 km), the imagettes are used to test the SCAT flagging for land and sea ice. We show that seemingly wrong SCAT measurements of wind speed can be explained by surface features.

TABLE I
COMPARISON OF DIFFERENT ENVISAT ASAR AND ERS SAR WAVE MODE PARAMETERS

	ERS-1/2	ENVISAT
radar frequency	5.300 GHz	5.331 GHz
polarization	VV	HH or VV
sampling	every 200 km	every 100 km
coverage	≈ 10x5 km	6x5 km - 10x5 km
daily coverage	≈ 1100 imagettes	≈ 2200 imagettes
incidence angle	19.3 / 23.5	14.1 - 42.3
R/V	110 s / 112 s	108 s - 142 s

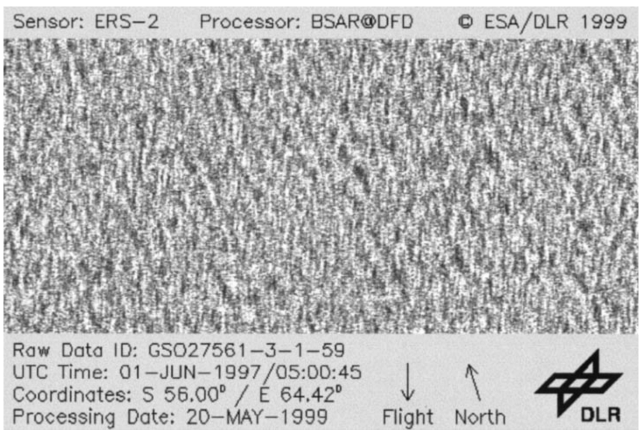

Fig. 1. Amplitude of a complex 10 × 6 km ERS-2 SAR imagette acquired on June 1, 1997, 05:00 UTC. The corresponding complex data were processed with the DLR processor BSAR.

3) Several new algorithms have been developed to derive wind speed and ocean wave spectra from complex SAR images by using cross-spectral methods. We use this dataset for a first global evaluation of these algorithms. The results are compared to ECMWF model and collocated SCAT data.

The paper is organized as follows. In the first section, SAR wave mode processing is discussed and global image statistics are given for a new dataset. Wind speed is evaluated globally, and the influence of surface features on wind speed is examined. The results are compared to SCAT wind measurements, and the quality of SCAT flagging for sea ice is evaluated. Finally, cross spectra are calculated to derive sea state and ocean wave propagation direction by multilook techniques.

II. SAR WAVE MODE PROCESSING

In this section, some general features of complex SAR data are discussed. Based on this, problems encountered in complex wave mode processing are analyzed.

A SAR achieves its high azimuthal resolution by recording the Doppler history of the returned signals [15]. Consider a single stationary point scatterer located at Doppler zero time $t_0 = 0$. As shown in Fig. 2(a), the corresponding SAR raw data are then given by a quadratic chirp (neglecting range migration) with envelope maximum located at Doppler centroid time t_c. Rather than focusing the entire chirp to a single image, subintervals of the integration time are often used to process looks with lower azimuthal resolution. In the case of the ERS SAR, the integration time is about 0.8 s. In this study, two looks with nonoverlapping frequency bands are used, each of which has an integration time of about 0.4 s and a separation time of the same order.

SAR processing is performed by matched filtering, which corresponds to a multiplication operation in the Fourier domain. Fig. 2(b) shows the phase of the raw data spectrum (solid), which is again a quadratic chirp. This spectrum is multiplied with the complex conjugate matched filter spectrum, removing the quadratic phase component. The dashed line in Fig. 2(b) is the phase of the complex image spectrum obtained after this processing step. Fig. 2(c) shows the resulting point scatterer response in the SAR intensity image using the entire bandwidth (solid) and the half bandwidth (dashed).

However, SAR imaging of a moving water surface is more complex. Considering again a single backscattering facette on the ocean surface, the following effects must be taken into account.

1) A velocity component of the facette in slant range direction leads to a Doppler shift and therefore to a shift of the corresponding image point in azimuth (velocity bunching, [16]).
2) Similarly, acceleration of the facette in slant range direction causes azimuthal smearing of the SAR image response (acceleration smearing, [4]).
3) Internal movement of the cross section pattern, e.g., caused by propagating ocean waves, leads to degraded resolution of the corresponding pattern in the SAR image. The movement can be analyzed using azimuth multilooking [13].
4) A lifetime of the facette shorter than the SAR integration time causes degraded azimuthal resolution. (coherence time, [17]).

A geometrical depiction of the velocity bunching and acceleration smearing effect is given in Fig. 3.

As SAR data are sampled with a finite pulse repetition frequency (PRF), only a limited bandwidth can be used for the matched filter. In order to maximize the SNR, it is important [18] to center the filter pass band at the Doppler centroid frequency f_{dc} [see Fig. 2(b)]. For this reason, an accurate f_{dc} estimation is a necessary step in SAR processing. This implies in particular Doppler ambiguity resolving. Fig. 4 shows that some care must be taken in this respect. Doppler centroid estimates are given in baseband for a global ERS-2 imagette dataset. As one can see, f_{dc} is passing through adjacent PRF bands at several locations. Wrong selection of the PRF band would lead to inaccurate range migration correction and defocusing of the imagettes.

Although several Doppler ambiguity resolving algorithms exist that deal with low contrast scenes [18]–[20], they usually require a significant amount of SAR signal samples to be analyzed exceeding by far the ERS wave mode cell size of about 2400 range lines with 528 range-compressed samples each. Thus, the Doppler ambiguity resolving still must be regarded as an open issue for ERS and ASAR wave mode data processing.

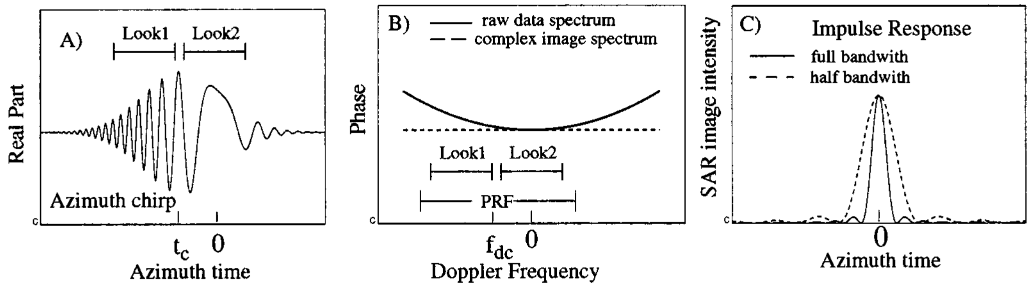

Fig. 2. (a) Azimuth chirp of single point scatterer in SAR raw data. Rather than using the entire integration time for processing a single image, subintervals can be selected to generate different looks with lower azimuth resolution. (b) Phase of raw data azimuth spectrum (solid) and complex image azimuth spectrum (dashed). Frequency bands of looks are indicated. The processed bandwidth is limited by the pulse repetition frequency (PRF). (c) Azimuth impulse response in SAR intensity image using the entire bandwidth (solid) and half bandwidth (dashed).

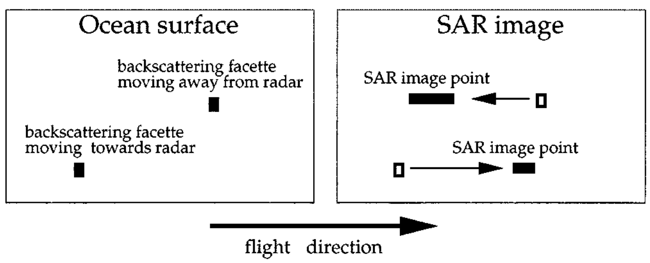

Fig. 3. Illustration of the velocity bunching and acceleration smearing effect. Two backscattering facettes on the ocean surface moving toward the radar and moving away from the radar are shown. The corresponding SAR image points are shifted and smeared in flight direction. The upper facette is assumed to have a smaller velocity and higher acceleration than the lower facette.

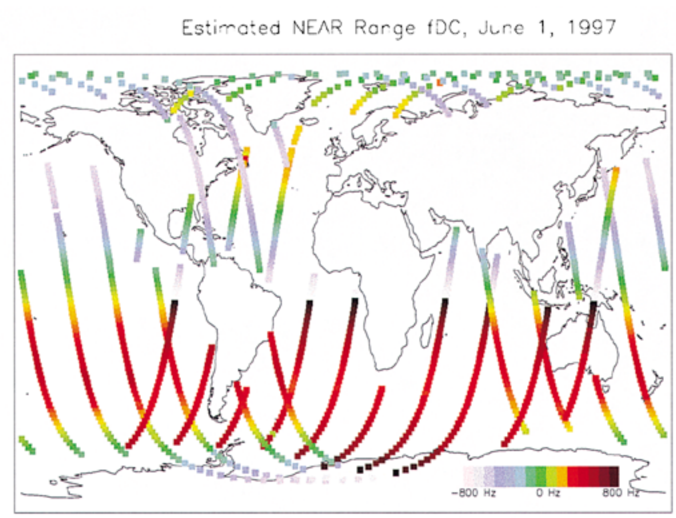

Fig. 4. Base band estimates of Doppler centroid for a global ERS-2 imagette data set acquired on June 1, 1997.

An analysis of about 25 000 ERS-1 and 6000 ERS-2 SAR image mode products produced at the German PAF showed that the ERS image mode Doppler values obtained during the nominal ERS operation in yaw-steering mode (i.e., maneuver situations excluded) follow a nominal behavior around an orbit. Therefore, a Doppler prediction table containing the expected Doppler value as a function of the geographical latitude for ascending and descending orbits is incorporated into BSAR and used for the Doppler ambiguity resolving.

An important extension to BSAR to complex wave mode data processing consists of the incorporation of a range-expansion step. Since BSAR uses the chirp scaling algorithm [21], [22], the onboard range-compressed wave mode data must be expanded into chirp raw data required as input for the chirp scaling algorithm.

Moreover, the ERS onboard range compression, achieved by a dispersive surface acoustic wave delay line (SAW), causes an additional range time delay with respect to the ERS image mode. This value is reported by ESA as 43.5 ms. A first measurement of this time delay is done using the corner reflector of the ERS-2 wave validation scene acquired on July 29, 1995, 21:46:44 UTC, kindly provided by ESA.

Since the Doppler frequency rate is range-time dependent, a wrong value for the electronic time delay leads to the assumption of a wrong range time and thus a degradation in the measured azimuth resolution of the corner reflector. The best azimuth resolution is obtained for an assumed additional SAW delay of 44.0 ms.

Also, the cross-correlation method described in Section V incorporates the possibility of determining time delay, since again, a wrong value for the range time leads to a wrong Doppler frequency rate and thus to a measured movement of the corner reflector. This measurement confirms the value of 44.0 ms.

III. Global Image Statistics

A. Moments of Intensity Images

In this chapter, some statistical properties of complex SAR images relevant for wind and wave measurements are given. Furthermore it is explained how azimuth and range multilook techniques can improve the estimation of statistical parameters of the underlying radar cross section.

Radar signals returned from different scatterers within a SAR resolution cell add up coherently as in a random walk. As there are many scatterers with uncorrelated complex reflectivities contributing, real and imaginary parts of a complex SAR image are independent Gaussian distributed. Hence, the intensity I of a single look complex pixel follows a negative exponential distribution [15]. A basic property of this distribution is that the variance $\mathrm{var}(I)$ equals the squared mean $\langle I \rangle^2$. SAR image statistics is commonly explained using a multiplicative noise model. SAR image intensity I is expressed as the product of a negative exponential distributed speckle process S with unit

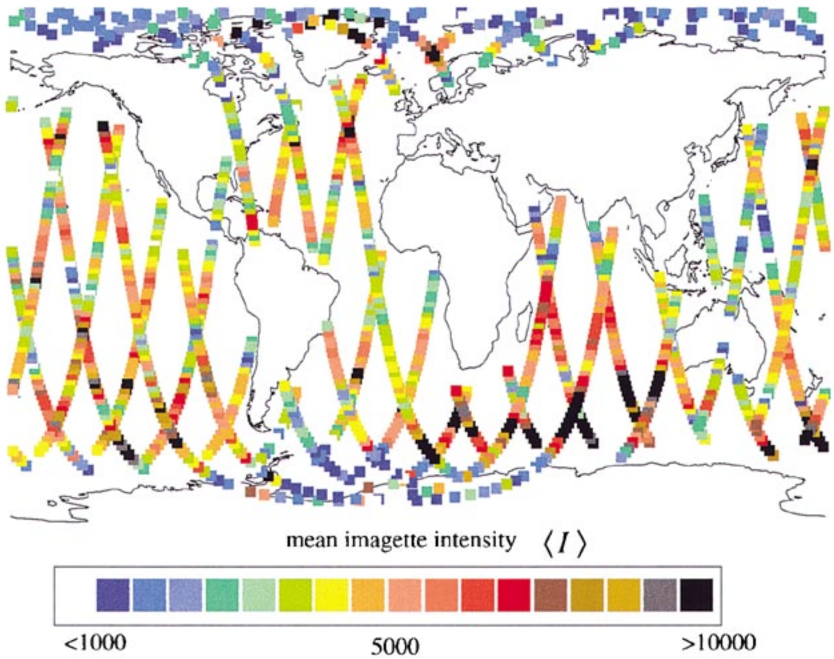

Fig. 5. Global distribution of mean imagette intensities for June 1–2, 1997.

mean and a process X carrying the cross section information [23]. Both processes are assumed to be independent

$$I = XS. \tag{1}$$

For a SAR image acquired over the ocean, X is modulated by the underlying radar cross section of the sea surface. To gain information about the sea surface requires estimation of statistical parameters of the process X. Therefore, it must be investigated how these parameters are related to the speckled measurement I. The mean of X, which is, for example, relevant for wind speed measurements, is simply given by

$$\langle X \rangle = \langle I \rangle. \tag{2}$$

Fig. 5 shows the global distribution of the (relatively calibrated) mean $\langle I \rangle$ derived from ERS-2 imagettes acquired on June 1, 1997. Low mean values occur over ice and on imagettes with low wind speed that may be contaminated by surface slicks (see Fig. 7). High mean values occur for imagettes taken in the strong storms near Antarctica. One commonly used algorithm to derive wind speed over the open ocean from mean backscatter is the so-called CMOD4, discussed in the next section. For accurate derivation of wind speed from mean backscatter, wind direction is needed as an additional input though. For the second moments, which are, e.g., used for ocean wave measurements, the situation is more complex. In this context, it is useful to introduce the modulation m of X

$$m = \frac{X - \langle X \rangle}{\langle X \rangle}. \tag{3}$$

It is convenient to use m as basis for wind or wave measurements [4], because no calibration of the SAR data is needed in this approach. In order to derive information on sea state, the covariance function ρ_{mm} is considered The covariance functions of m and I are connected by the following expression [12]:

$$\frac{\rho_{II}}{\langle I \rangle^2} = \rho_{mm}(\rho_{SS} + 1) + \rho_{SS}. \tag{4}$$

The corresponding variance spectrum Φ_I then follows by taking the Fourier transform of (4).

$$\Phi_I = \langle I \rangle^2 (\Phi_m + \Phi_S + \Phi_m * \Phi_S). \tag{5}$$

Here, $*$ denotes the convolution operator. The last two equations show that due to speckle contribution, it is not straightforward to derive the second moments of X from the measurement I. In particular, this requires some knowledge about the spectrum of the speckle process.

However, being only interested in the variance of m [$\mathrm{var}(m) = \rho_{mm}(0)$], the speckle problem becomes more straightforward. In the case of a single look image, $\mathrm{var}(m)$ is related to the coefficient of variance (CVAR), often used in SAR image analysis [12] by

$$\mathrm{CVAR} = \frac{\mathrm{var}(I)}{\langle I \rangle^2} = 1 + 2\mathrm{var}(m). \tag{6}$$

In practice, $\mathrm{var}(m)$ can be estimated by using (6). Fig. 6 shows the global distribution of $\mathrm{var}(m)$ derived from ERS-2 imagettes acquired on June 1, 1997. It can be observed that $\mathrm{var}(m)$ is close to zero almost all over the ocean, showing maximum values of up to 0.1 in areas of strong wind, e.g., near Antarctica. Larger values are found for images that show surface features. It seems that $\mathrm{var}(m)$ could be a good measure for sea ice type, showing strong variance between zero and 0.2 in the sea ice region. Near Antarctica, imagettes showing either the ocean surface in strong wind speed or sea ice have similar values of $\mathrm{var}(m)$, so that

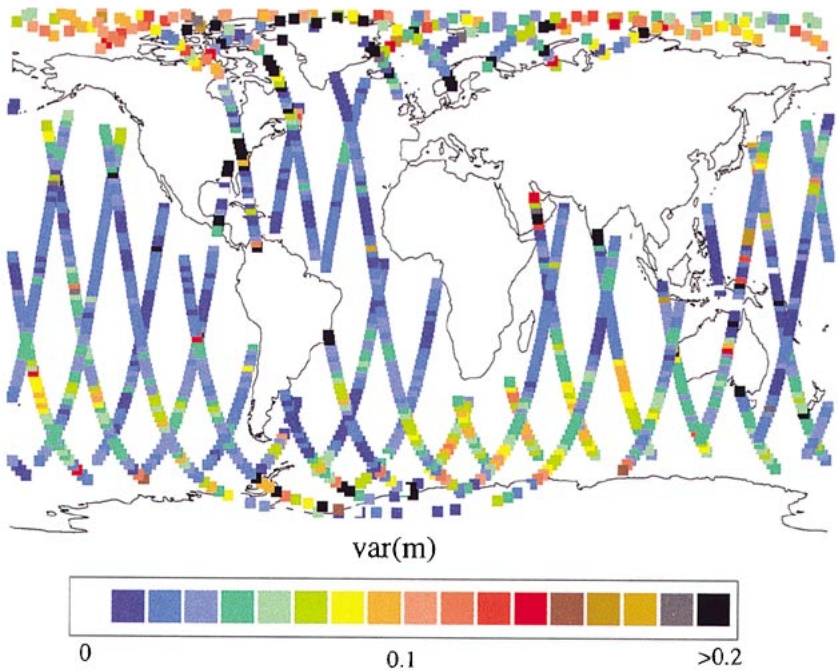

Fig. 6. Variance of the modulation of X calculated for a global dataset of complex imagettes acquired on June 1–2, 1997.

more sophisticated parameters are needed to discriminate between them.

B. Derivation of Second Moments Using Complex Data

To overcome the problems encountered above in the computation of the second moments of X, complex SAR images are very useful. The idea is to use two looks I_1, I_2 extracted from the range or azimuth spectrum of the complex image. Due to the reduced bandwidth, looks have a degraded resolution in range or azimuth. In the case of nonoverlapping frequency bands (compare Fig. 2), the looks are affected by uncorrelated speckle processes S_1 and S_2. This means

$$I_i = XS_i \quad i = 1, 2 \tag{7}$$

for the range look case and

$$I_i = X_iS_i \quad i = 1, 2 \tag{8}$$

when using azimuth looks. The difference is made because on the time scale relevant for ocean wave measurements range looks can be regarded as simultaneous (the ERS chirp has a time span of about 40 μs). Azimuth looks on the other hand are about 0.4 s apart, so that the change of cross section taking place during look acquisitions is not negligible. The range look cross-covariance function is related to the covariance function of X by

$$\rho_{I_1I_2}(k) = \rho_X(k). \tag{9}$$

For azimuth looks, the corresponding relation is given by

$$\rho_{I_1I_2}(k) = \rho_{X_1X_2}(k). \tag{10}$$

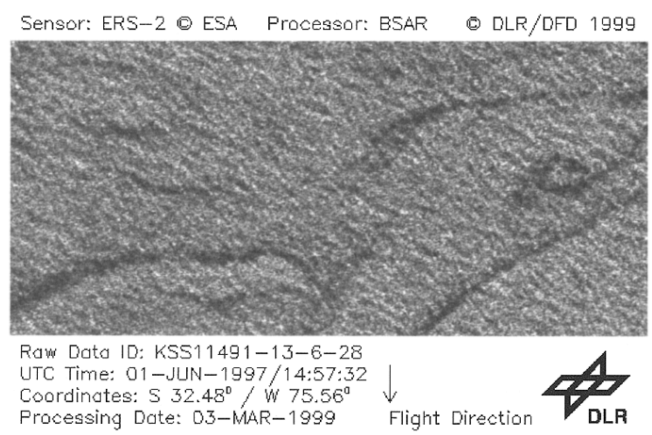

Fig. 7. Amplitude of a complex ERS-2 imagette acquired on June 1, 1997, showing slicks on the ocean surface.

Both equations show that the speckle contribution cancels out. The multilook technique thus offers a straightforward way to estimate parameters of the process X. As an illustration, Fig. 8 shows the azimuthal autocorrelation function of an ERS-2 imagette (dashed). The function shows a strong peak in the center caused by speckle. The solid line represents the cross-correlation function (CCF) of two range looks computed from the complex imagette. As one can see the speckle bias is removed, leaving the smoother autocorrelation function of the underlying cross section pattern X. A comparison between the azimuth CCF derived from range (solid) and azimuth (dashed-dotted) looks is given in Fig. 9. Both correlation functions show an ocean wave system of about 150 m wavelength travelling in azimuth direction. The CCF of the azimuth looks indicates a small phase shift of the ocean waves taking place in about 0.5 s. Apart

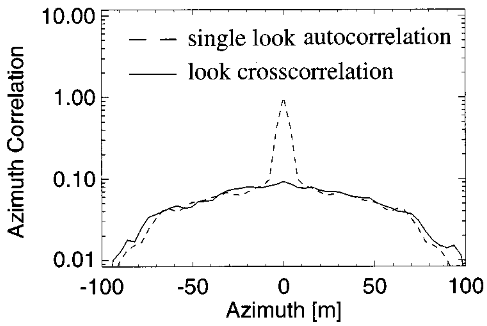

Fig. 8. Azimuth autocorrelation function of single look ERS-2 imagette (dashed) and cross-correlation function of two range looks (solid).

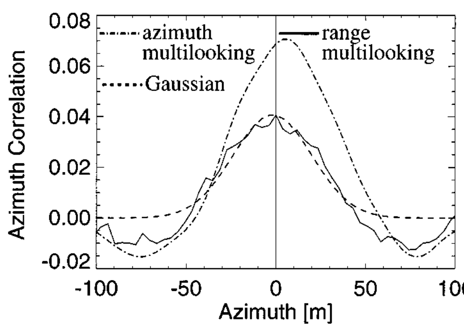

Fig. 9. Cross-correlation function of two looks extracted from the range spectrum (solid) and azimuth spectrum (dashed-dotted) of a complex ERS-2 imagette. The dashed line represents a Gaussian fitted to the range look cross-correlation function.

from that, it can be observed that due to the lower azimuthal resolution, the CCF is smoother for the azimuth look case.

In the following sections, different wind and wave measurement algorithms are presented, which take advantage of multilooking techniques.

IV. Wind Speed Measurements

A. CMOD Approach

In this section, the relation between single look imagette brightness and wind speed is analyzed. A similar analysis was carried out for three look averaged imagettes by Kerbaol [12].

Wind speeds from ERS SAR images of the ocean surface have been derived by Alpers and Brümmer [24], Chapron *et al.* [25], Rosenthal *et al.* [26], Horstmann *et al.* [27] and Scoon *et al.* [28].

The model of Wright [29] explains backscatter from the rough ocean surface for moderate incidence angles (20–60°) by resonant Bragg scattering. The backscatter signal is dominated by the ocean wave component in resonance with the incidence radiation. More precisely, the radar cross section σ_0 is related to the energy contained in the ocean wave component k_w, which lies in the incident plane and obeys the Bragg condition

$$k_w = 2k_{el} \sin \alpha. \tag{11}$$

Here, α is the incidence angle of the radar beam, and k_e is the electromagnetic wavenumber of the radar. In case of the ERS SAR, operating at C-band with incidence angles between

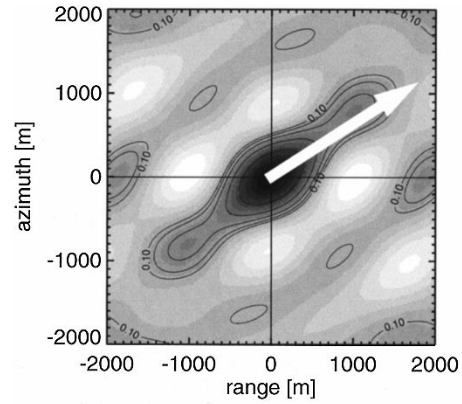

Fig. 10. Low-pass filtered 2-D autocorrelation function of ERS-2 imagette acquired on June 1, 1997, 05:00 UTC (compare Fig. 1). Wavelength shorter than 2 km are removed. The arrow indicates the wind direction determined by the ERS-2 SCAT. The measured wind speed is 16.4 m/s.

20–26°, Bragg waves have length in the range of 6.5–8.3 cm. Therefore, backscatter can be used to evaluate parameters which influence the small scale roughness, like the wind speed.

Grey levels of SAR images are converted into normalized calibrated radar cross-section (NCRS) using the ESA calibration algorithm [30]. For SAR image mode, some calibration problems occurred due to saturation of the ADC converter that occurred mainly over bright areas like inland ice or sea surface under strong wind conditions. These problems were solved by a recalibration procedure.

After calibration, wind speed is derived from the images using the semi-empirical CMOD4 algorithm [31], which was originally derived to retrieve wind speed and direction from scatterometer measurements. CMOD was developed for the ERS scatterometer, but as the ERS SCAT and the ERS SAR are both operating at C-Band, it can be used on SAR data as well [32]. As SAR images only yield one backscatter measurement for each pixel (contrary to the three σ_0 measurements from the three SCAT antennas), some additional information on wind direction is needed for the SAR. Usually, SAR images show distinct features like wind streaks or shadowing behind coasts, from which the wind direction can be derived.

On wave mode images, not as many distinct stripes show up as on near coastal images, which is probably due to higher turbulence in coastal areas. More sophisticated analysis is needed than the Fourier analysis used in [32] to derive wind direction. As an illustration, Fig. 10 shows the two-dimensional (2-D) autocorrelation function computed from the imagette shown in Fig. 1. To focus on large scale image structures, which are not due to ocean waves, wavelengths below 2000 m were removed. The arrow indicates the wind direction derived from the collocated SCAT measurement. As can be seen, there is a good correspondence between the orientation of the large scale image structures and the measured wind direction. Visual inspection showed that this kind of agreement can be found in about 40% of the cases.

Up to now, BSAR wave mode is only relatively calibrated. As ERS wave mode is even more severely affected by ADC saturation than image mode, absolute calibration for very strong wind conditions will be difficult to achieve for ERS SAR. However,

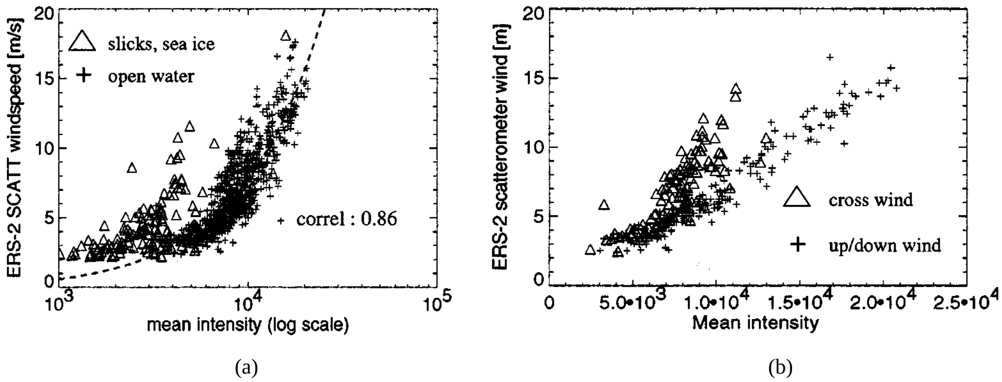

Fig. 11. (a) Mean intensity versus ERS SCAT wind speed for homogeneous imagettes (+) and imagettes affected by slicks, sea ice, or atmospheric phenomena ($\triangle$). (b) Mean intensity versus ERS SCAT wind speed for up/down wind (+) and cross wind ($\triangle$).

for the next generation of data from the ENVISAT satellite, saturation will be no longer a problem.

Fig. 11(a) shows a scatter plot of mean intensity (log scale) versus scatterometer wind speeds. Triangles indicate imagettes on which sea ice, slicks, or atmospheric effects were found by inspection. As can be seen, these imagettes are characterized by relatively low intensities. In addition, it can be observed that most of the corresponding SCAT wind speeds are also on the lower level, suggesting that the phenomena seen on the imagettes correspond to low wind speed. Slicks are empirically modeled in CMOD4 since the occurrence of slicks in the ERS scatterometer footprint is strongly correlated with the wind speed magnitude (i.e., slicks disappear at moderate wind speeds). The other geophysical anomalies are flagged in the ERS scatterometer processing [33]. The linear regression line (dashed) was computed for the remaining homogeneous imagettes. The corresponding correlation coefficient is 0.86. Fig. 11(b) shows mean imagette intensity versus SCAT wind speed for cross wind ($\triangle$) and up/down wind (+) respectively, where wind direction is also taken from the ERS-2 SCAT. Only wind directions with a maximum deviation of 25° from range and azimuth direction, respectively, are used in this plot. As predicted by the CMOD model, it clearly shows up that the imagette intensities are higher for up/downwind than cross wind given the same wind speed.

In a next step, the wave mode will be calibrated and the wind streak algorithm refined. The above results strongly suggest that CMOD applied to the ERS wave mode will yield a reliable and stable wind speed algorithm as well.

B. Cross-Correlation Algorithm

In this section, a new cross-correlation wind speed algorithm is derived using range multilooking. The azimuthal cross-correlation algorithm (CCA), developed by [12], is applied to the dataset of the complex imagettes also. The CCA algorithm is based on the azimuthal low pass character of the SAR ocean wave imaging process, which is caused by sea surface motion. The basic mechanism is an azimuthal shift and smearing of SAR image points due to slant range velocity and acceleration components of the backscattering facettes (compare Fig. 3).

In the spectral domain, SAR ocean wave imaging can be described to first order by a quasilinear model for the variance spectrum $\Phi_m(k)$ of the modulation m [4]

$$\Phi_m(k) = \exp\left(-k_x^2 \rho_\xi(0)\right) \left(\left|T_k^{SAR}\right|^2 F_k + \left|T_{-k}^{SAR}\right|^2 F_{-k}\right). \tag{12}$$

Here, F is the ocean wave spectrum, T^{SAR} a transfer function, and k_x is the azimuthal wavenumber component. For the definition of m, see (3). The width of the exponential factor is controlled by the variance of the azimuthal image point shift $\rho_\xi(0)$. Assuming small incidence angles, $\rho_\xi(0)$ can (to first order) be expressed in terms of the ocean wave frequency spectrum $S(\omega)$, slant range R, and platform velocity V

$$\rho_\xi(0) = \left(\frac{R}{V}\right)^2 \int_0^\infty \omega^2 S(\omega)\, d\omega. \tag{13}$$

The idea of the CCA algorithm is to use the dependence of $S(\omega)$ and hence, $\rho_\xi(0)$ on wind speed. As other parameters like wave age or swell wave height have an impact, too [6], the CCA algorithm should not be applied under fetch-limited or swell-dominated conditions. To estimate $\rho_\xi(0)$, a strong simplification is made, namely, that the second factor in (12) (in brackets) can be regarded as constant. In that case, the azimuthal auto covariance function $\rho_m = F^{-1}(\Phi_m)$ is Gaussian as well

$$\rho_m(x) \sim \exp\left(-\pi \frac{x^2}{\lambda^2}\right). \tag{14}$$

Here, λ is defined as the cutoff wavelength in the spatial domain. Other techniques have been proposed, which estimate the cutoff wavelength in the spectral domain fitting more sophisticated models [6].

Fig. 12 shows the performance of the CCA algorithm applied to the complex imagette data set using multilooks in range. To get rid of the speckle peak in the CCA algorithm and to obtain a better performance of the fit procedure, it was proposed in [12] to use the cross correlation between different looks having uncorrelated speckle noise. However, in contrast to the proposed method, which uses azimuth multilooking, in this study, looks extracted from the range chirp spectrum are used. This approach has two advantages: the azimuth resolution is not degraded and the cross-correlation function is not distorted by the phase shift of long azimuth ocean waves.

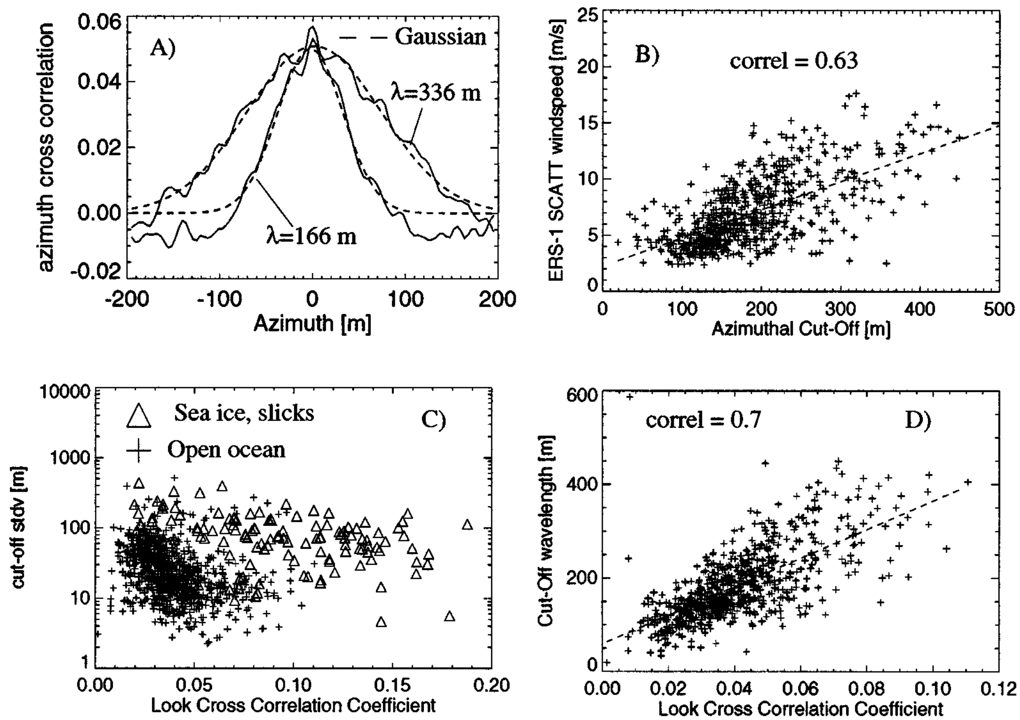

Fig. 12. (a) Azimuth cross-correlation function of two ERS-2 imagettes acquired on June 1, 1996, at $-54.311°$ lat, $65.577°$ lon and $-23.048°$ lat, $262.061°$ lon, respectively. Fitted Gaussians indicating 336 m and 166 m cutoff wavelength are plotted in dashes. (b) Scatter plot of cutoff wavelength versus SCAT wind speed, with regression plotted in dashes. (c) Scatter plot of look cross-correlation coefficient versus cutoff standard deviation. Triangles mark imagettes with detected sea ice, slicks, or atmospheric phenomena. Crosses indicate homogeneous imagette. (d) Scatter plot of cross-correlation coefficient versus cutoff wavelength with regression line plotted in dashes.

The Gaussian fit procedure for the range CCA model given by (14) is demonstrated in Fig. 12(a). The cross-correlation functions of two imagettes are shown together with fitted Gaussians, indicating 336 m and 166 m cutoff wavelength, respectively. The interval [-200 m, 200 m] of the azimuth axis was used for the fit procedure.

To analyze the wind speed dependence of λ, simultaneous measurements of the ERS-2 scatterometer are used. To check for the homogeneity of the imagette and the stability of the fit procedure, λ was not only estimated for the area of the entire imagette, but also for quarter subimages. Fig. 12(c) shows the respective standard deviation of λ calculated for each imagette versus the look cross-correlation coefficient. Triangles correspond to imagettes on which sea ice, slicks, or atmospheric phenomena were found by inspection, whereas crosses mark homogeneous imagettes. It seems that these parameters allow a considerably good discrimination of the two imagette classes.

Fig. 12(b) shows a scatter plot of the cutoff wavelength versus SCAT wind speed with regression line plotted by a dashed line. Only imagettes with standard deviation λ smaller than 50 m were used for the plot. The correlation coefficient of 0.63 indicates a reasonably close relationship. However, the CCA method must be further improved to obtain sufficient accuracy. This implies in particular a better understanding of the shape of the SAR spectrum and its dependence on wind speed. Fig. 12(d) shows an interesting relation between cross-correlation coefficient and cutoff wavenumber. As can be seen, the cutoff increases with higher cross-correlation values. In the spectral domain, this simply means that SAR image spectra with high energy are more strongly affected by azimuthal low pass filtering. This relation can be explained using the quasi-linear model given in (12). High energies in the SAR spectrum are due to high sea states, which in turn lead to long azimuthal image point shifts $\rho_\xi(0)$ and hence short cutoff wavelengths λ.

V. SAR Cross Spectra

In this section, the SAR cross-spectrum technique is used to derive the ocean wave propagation direction. As explained in Section III, this method has the advantage of removing the speckle bias. In addition, the cross-spectrum of azimuth looks can be used to detect the phase shift of ocean waves taking place between look acquisitions [13].

As in the ordinary SAR power spectrum, the cross-spectrum is affected by a nonlinear imaging mechanism too. Derivation of ocean wave spectra from cross spectra therefore requires inversion techniques using some kind of *a priori* knowledge [13]. In this study, a first assessment of the statistical properties of a global set of cross spectra is presented. Inversion techniques are not analyzed here but are the subject of a separate paper.

For first order, the cross-spectrum $\Phi_{m_1 m_2}(k)$ can be expressed by the following quasilinear model:

$$\begin{aligned}\Phi_{m_1 m_2}(k) = \exp\left(-k_x^2 \rho_\xi(0)\right) \\ \cdot \Big(\exp(i\omega\Delta t)\left|T_k^S\right|^2 F_k \\ + \exp(-i\omega\Delta t)\left|T_{-k}^S\right|^2 F_{-k}\Big). \quad (15)\end{aligned}$$

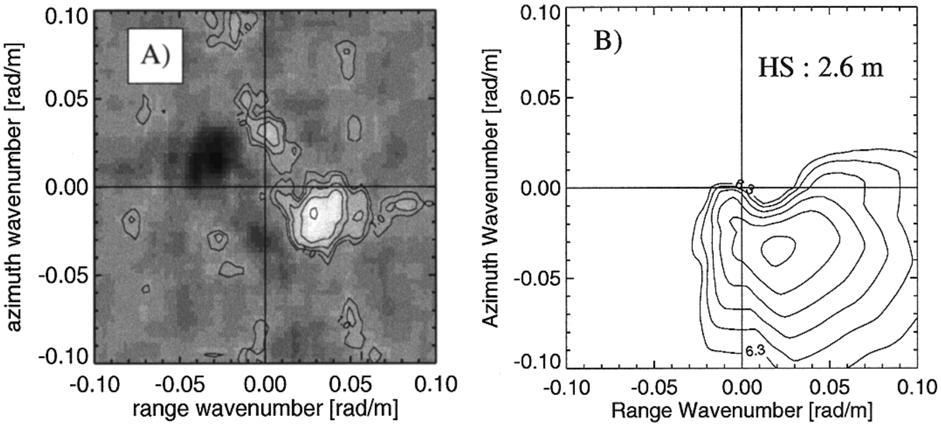

Fig. 13. (a) Complex part of cross-spectrum computed from complex ERS-2 imagette acquired on June 1, 1997 06:27 UTC at latitude $-8.8°$ longitude $56.51°$ (b) ECMWF ocean wave spectrum with 2.6 m significant wave height computed for June 1, 1997 06:00, $-9°$ lat $56.63°$ lon.

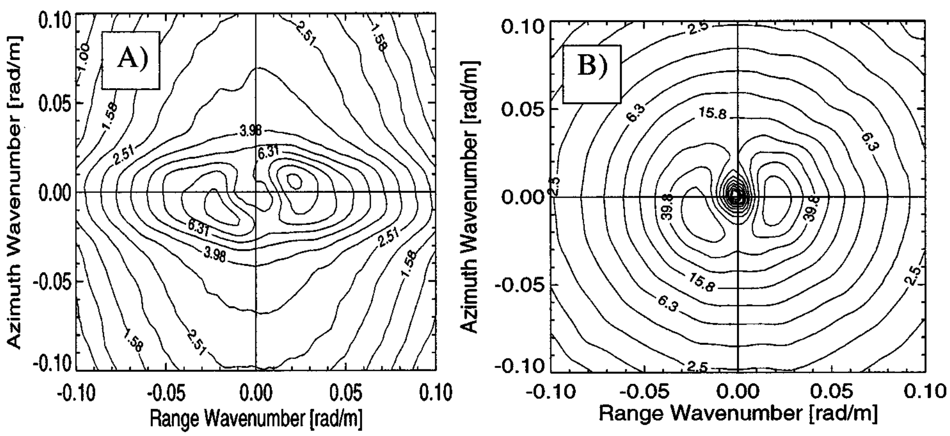

Fig. 14. (a) Average cross-spectrum energy derived from $n = 1089$ ERS-2 imagettes. (b) Average ocean wave spectrum derived from $n = 1089$ imagette collocated ECMWF spectra.

Here, Δt is the look separation time, which is of the order of 0.4 s in this analysis, and ω is the ocean wave frequency, which is related to the wavenumber k by the dispersion relationship

$$\omega^2 = gk \tanh(kh) \tag{16}$$

with h water depth and g constant of gravity.

Fig. 13(a) shows an example of the cross-spectrum method. Fig. 13(b) shows the imaginary part of the azimuth look cross-spectrum derived from an ERS-2 imagette acquired on June 1, 1997, 06 : 27 UTC, indicating a wavesystem of about 200 m length propagating to the right. In Fig. 13(b), the collocated ECMWF wave spectrum with 2.6 m significant wave height is plotted, confirming the SAR observation.

The imagette cross spectra were analyzed on a statistical basis using all imagettes with collocated ECMWF ocean wave spectra ($n = 1089$). The time gap between SAR observations and model spectra is less than 3 h, and the spatial distance is less than 100 km. Fig. 14(a) shows the average cross-spectrum energy computed as

$$\zeta(k) = \frac{1}{n} \sum_{\mathrm{im}(\Phi^i(k))>0} \left|\Phi^i_{m_1 m_2}(k)\right|. \tag{17}$$

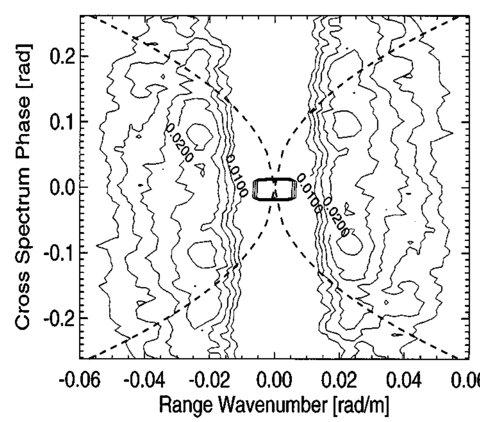

Fig. 15. Distribution of energy of the cross-spectrum in the range wavenumber/phase plane. The dashed lines represent the theoretical phase for ocean waves propagating in deep water.

The azimuthal low pass filtering of the cross spectra (15) is clearly visible. In addition, the average spectrum is nearly symmetric, indicating wavesystems of about 300 m wavelength propagating in approximate range direction. The corresponding average ECMWF ocean wave spectrum is given in Fig. 14(b), showing reasonable agreement with the observed cross spectra.

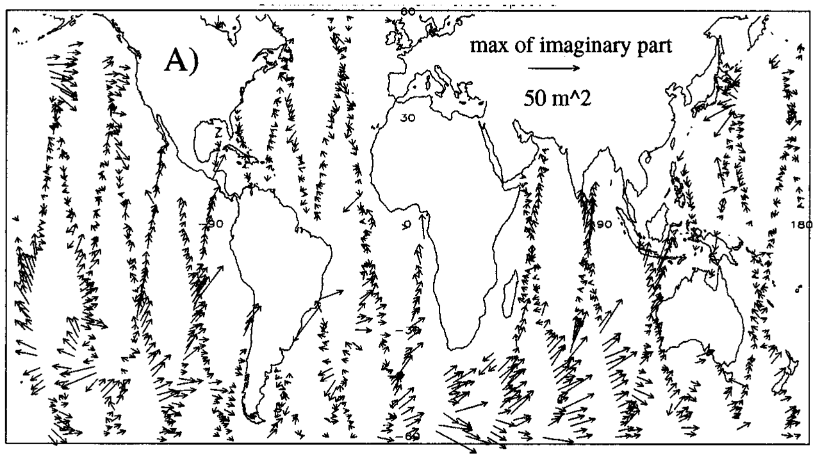

Fig. 16. Global map of ERS-2 imagette derived wave propagation directions on June 1, 1997. Arrow length corresponds to maximum of cross-spectrum imaginary part.

To study the phase of the measured cross spectrum, the energy distribution over the interval [0, 2 π] was analyzed. To avoid distortions caused by velocity bunching effects, the analysis is concentrated on the phase observed along the range axis of the cross spectrum. Fig. 15 shows the distribution of the cross-spectrum energy $|\Phi_{m_1 m_2}|$ in the range wavenumber/phase plane. The dashed lines represents the phase expected for ocean waves propagating in very deep water (16). The phases scatter considerably, showing four weak local maxima at a wavenumber of ± 0.025 rad/m and phase values of ± 1 rad and ± 0.8 rad, respectively. The location of the local maxima with respect to the dashed line shows that the phase shift of range waves derived from the ERS imagettes tends to be smaller than predicted by the deep water dispersion relation.

This leads to the question of whether, despite of the strong scattering in the phase of the cross-spectrum phase, a reasonable resolution of wave propagation ambiguity can be achieved. The problem is analyzed by studying the cross correlation of the cross-spectrum imaginary part (> 0) and the collocated ECMWF spectrum from the WAM model [34]. Only one-dimensional (1-D) spectra obtained by averaging over range and azimuth respectively are considered. Fig. 17 shows the analysis of the cross-spectrum for one day of complex data. The global distribution of detected wave propagation directions for June 1, 1997, is shown in Fig. 16(a). The directions were derived by determination of the maximum in the cross-spectrum imaginary part. The arrow lengths correspond to the respective maximum values. Fig. 17(a) shows a contour plot of the cross correlation between the range cross-spectrum imaginary part (> 0), and the corresponding range wave spectrum. It can be seen that the highest correlations are found along the diagonal plotted in dashed, while negative correlations are found in the upper left and bottom right quarter. Although the absolute correlation values are relatively small, showing a maximum of about 0.6, this pattern indicates a reasonable propagation direction ambiguity resolution for waves travelling in range direction. For the azimuth case, Fig. 17(b) shows a similar behavior, although the correlation pattern is more stretched in the azimuth direction of the ECMWF wave spectrum. This is due to the velocity bunching mechanism, which causes short wave systems traveling in the azimuth direction to be shifted toward lower azimuth wavenumbers in the SAR spectrum.

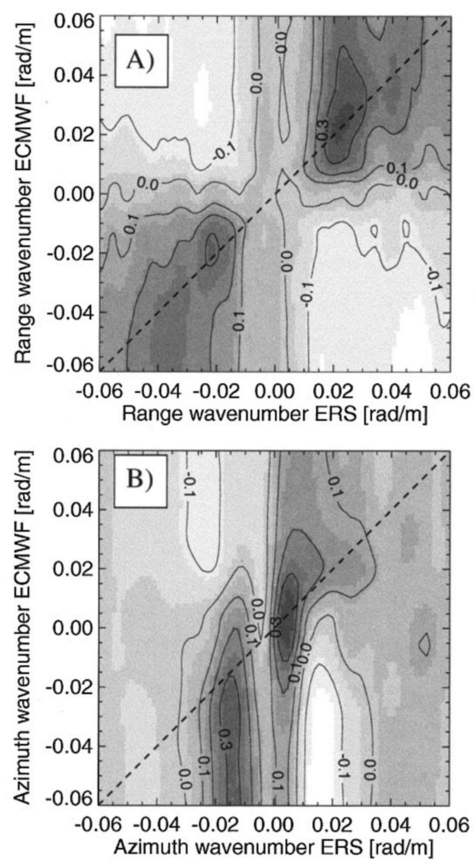

Fig. 17. (a) Cross correlation in range direction between cross-spectrum imaginary part (> 0) and collocated ECMWF ocean wave spectrum. (b) Cross correlation in azimuth direction between cross-spectrum imaginary part (>0) and collocated ECMWF ocean wave spectrum.

VI. Summary and Conclusions

In the present study, a first statistical analysis of wind and wave measurement techniques using complex ERS-2 imagette data is given. The study shows both the potential as well as the limitations of these methods.

Two techniques were applied to derive wind speed from imagettes. The CMOD technique relies on the mean image intensity and shows good results. The performance of the technique will become even better if some prior information about the wind vector is used and the imagettes is properly calibrated. The impact of phenomena like slicks, sea ice, or atmospheric processes on the CMOD method was analyzed. There is some evidence that collocated ERS SCAT measurements are affected by these phenomena. These effects are taken into account in scatterometer processing and quality control.

The CCA method is based on the analysis of the azimuth correlation function. Range multilooking is used to remove the speckle bias. Inhomogeneities detected on imagettes are taken into account. The correlation between the measured image smearing in azimuth and collocated SCAT wind measurements is reasonable. However, the method does not seem to be able to compete with the CMOD algorithm.

Ocean waves are studied using the cross-spectrum technique. A good agreement is found between wave propagation directions derived from complex imagettes and collocated ECMWF wave spectra. Considerable scattering of the cross-spectrum phase was observed, showing small agreement with theoretical predictions. It must be further investigated whether this behavior is a natural limitation of the cross-spectrum technique or if the performance can be improved by applying more sophisticated processing techniques.

The present study is one preparation step for the planned operational use of ENVISAT imagettes at meteorological centers like ECMWF.

Acknowledgment

The authors would like to thank the European Space Agency (ESA), Noordwijk, The Netherlands, for providing ERS-2 SAR wave mode raw data in the framework of the ERS A03 project COMPLEX (ID 192). They would also like to thank the European Center for Medium Range Weather Forecast (ECMWF), Reading, U.K., for providing collocated ocean wave model data.

References

[1] P. Heimbach, S. Hasselmann, and K. Hasselmann, "Statistical analysis and intercomparison with WAM model data of three years of global ERS-1 SAR wave Mode Spectral retrievals," *J. Geophys. Res.*, vol. 103, pp. 7931–7977, 1998.

[2] W. R. Alpers, D. B. Ross, and C. L. Rufenach, "On the detectability of ocean surface waves by real and synthetic aperture radar," *J. Geophys. Res.*, vol. 86, pp. 6481–6498, 1981.

[3] H. Krogstad, O. Samset, and P. W. Vachon, "Generalizations of the nonlinear ocean-SAR transformation and a simplified SAR inversion algorithm," *Atmos. Ocean.*, vol. 32, pp. 61–82, 1994.

[4] K. Hasselmann and S. Hasselmann, "On the nonlinear mapping of an ocean wave spectrum into a synthetic aperture radar image spectrum," *J. Geophys. Res.*, vol. 96, pp. 10 713–10729, 1991.

[5] H. Krogstad, "A simple derivation of Hasselmann's nonlinear ocean-synthetic aperture radar transform," *J. Geophys. Res.*, vol. 97, pp. 2421–2425, 1992.

[6] P. W. Vachon and H. E. Krogstad, "Airborne and spaceborne synthetic aperture radar observations of ocean waves," *Atmos. Ocean.*, pp. 83–112, 1994.

[7] "Advances in oceanography and sea ice research using ERS observations," *J. Geophys. Res.*, vol. 103, no. C4, 1998.

[8] L. A. Breivik, M. Reistad, H. Schyberg, J. Sunde, H. E. Krogstad, and H. Johnson, "Assimilation of ERS SAR wave spectra in an operational wave model," *J. Geophys. Res.*, vol. 103, pp. 7887–7900, 1998.

[9] C. Mastenbroek and C. F. Valk, "Wave spectra from SAR imagettes," *J. Geophys. Res.*, vol. 101, 1996.

[10] C. Mastenbroek and C. F. de Valk, "A semi-parametric algorithm to retrieve ocean wave spectra from SAR," *J. Geophys. Res.*, vol. 103, 1998.

[11] G. Brooker, "UWA processing algorithm specification, version 2.0," Tech. Rep., Eur. Space Agency, ESTEC/NWP, Noordwijk, The Netherlands, 1995.

[12] V. Kerbaol, B. Chapron, and P. W. Vachon, "Analysis of ERS-1/2 synthetic aperture radar wave mode imagettes," *J. Geophys. Res.*, vol. 103, pp. 7833–7846, 1998.

[13] G. Engen and H. Johnson, "SAR-ocean wave inversion using image cross spectra," *IEEE Trans. Geosci. Remote Sensing*, vol. 33, pp. 1047–1056, 1995.

[14] H. Johnsen and Y.-L. Desnos, "Expected performance of the ENVISAT ASAR wave mode cross spectra product," in *Proc. IGARSS '99 Conf.*, Hamburg, Germany, 1999.

[15] R. Bamler and B. Schättler, "SAR data acquisition and image formation," in *SAR Geocoding: Data and Systems*. Karlsruhe, Germany: Wichman, 1993.

[16] D. R. Lyzenga, R. A. Shuchman, and J. D. Lyden, "SAR imaging of waves in water and ice: evidence for velocity bunching," *J. Geophys. Res.*, vol. 90, pp. 1031–1036, 1985.

[17] R. E. Car, "Estimating ocean coherence time using dual-baseline interferometric synthetic aperture radar," *IEEE Trans. Geosci. Remote Sensing.*, vol. 32, pp. 846–854, July 1994.

[18] R. Bamler, "PRF-ambiguity resolving by wavelength diversity," *IEEE Trans. Geosci. Remote Sensing*, vol. 29, pp. 997–1001, 1991.

[19] ——, "Wavelength diversity PRF ambiguity resolver; calibration and test results for ERS-1 SAR," in *Proc. IGARSS'93 Conf.*, Tokyo, Japan, 1993.

[20] F. H. Wong and I. G. Cumming, "A combined SAR Doppler centroid estimation scheme based upon signal phase," *IEEE Trans. Geosci. Remote Sensing*, vol. 34, pp. 696–707, 1996.

[21] R. K. Raney, H. Runge, R. Bamler, I. G. Cumming, and F. H. Wong, "Precision SAR processing using chirp scaling," *IEEE Trans. Geosci. Remote Sensing*, vol. 32, pp. 786–799, 1994.

[22] H. Breit, B. Schättler, and U. Steinbrecher, "A high precision workstation-based chirp scaling SAR processor," in *Proc. IGARSS97 Conf.*, Singapore, 1997.

[23] W. Alpers and K. Hasselmann, "Spectral signal to clutter and thermal noise properties of ocean wave imaging synthetic aperture radars," *Int. J. Remote Sensing*, vol. 3, pp. 423–446, 1982.

[24] W. Alpers and B. Brümmer, "Atmospheric boundary layer rolls observed by the synthetic aperture radar aboard the ERS-1 satellite," *J. Geophys. Res.*, vol. 99, pp. 12 613–12 621, 1994.

[25] B. Chapron, T. Elfouhaily, and V. Kerbaol, "A SAR speckle wind algorithm," in *Proceedings of the 2nd ERS-1 Workshop*. Plouzane, France: Institut Francais de Recherche pour l'Exploitation de la Mer (IFREMER), 1994.

[26] W. Rosenthal, S. Lehner, J. Horstmann, and W. Koch, "Wind measurements using ERS-1 SAR," in *Proc. 2nd ERS Applications Workshop*, vol. SP-383, 1997, pp. 355–358.

[27] J. Horstmann, W. Koch, S. Lehner, and R. Tonboe, "Wind retrievals over the ocean using synthetic aperture radar with C-band HH polarization," *IEEE Trans. Geosci. Remote Sensing*, vol. 38, pp. 2122–2131, Sept. 2000.

[28] A. Scoon and I. S. Robinson, "Demonstration of an improved calibration scheme for ERS-1 SAR imagery using a scatterometer wind model," *Int. J. Remote Sensing*, 1995.

[29] J. W. Wright, "Backscattering from capillary waves with applications to sea clutter," *IEEE Trans. Antennas Propagat.*, vol. AP-14, pp. 749–754, 1966.

[30] H. Laur, P. Bally, P. Meadows, J. Sanchez, B. Schaettler, and E. Lopinto, "Derivation of the backscattering coefficient σ_0 in ESA ERS-1/2 SAR PRI data products," Tech. Rep., Rev. 1, Eur. Space Agency, Noordwijk, The Netherlands, 1996.

[31] A. Stoffelen and D. Anderson, "Characterization of ERS-1 scatterometer measurements and wind retrieval," in *Proc. 2nd ERS-1 Symp.—Space at the Service of our Environment*, Hamburg, Germany, 1993, ESA SP-361.

[32] S. Lehner, J. Horstmann, W. Koch, and W. Rosenthal, "Mesoscale wind measurements using recalibrated ERS SAR images," *J. Geophys. Res.*, vol. 103, pp. 7847–7856, 1998.

[33] A. Stoffelen, "Scatterometry," Ph.D. dissertation, Univ. Utrecht, Utrecht, The Netherlands, 1998.

[34] WAMDI Group, “The WAM model—A third generation ocean wave prediction model,” *J. Phys. Oceanogr.*, pp. 1775–1810, 1988.

Susanne Lehner received the M.Sc. degree in applied mathematics from Brunel University, Uxbridge, U.K., in 1979, and the Ph.D. degree in geophysics from the University of Hamburg, Hamburg, Germany, in 1984.

She was a Research Scientist, Max-Planck Institute for Climatology, Hamburg, Germany, and joined the German Aerospace Center (DLR/DFD), Oberpfaffenhofen, in 1996. Currently, she is a Research Scientist in marine remote sensing, Remote Sensing Technology Institute (DLR/IFM), Oberpfaffenhofen, Germany, working on the development of algorithms determining marine parameters from SAR.

Johannes Schulz-Stellenfleth received the Diploma degree in applied mathematics from the University of Hamburg, Hamburg, Germany, in 1996.

He joined the German Aerospace Center (DLR/DFD), Oberpfaffenhofen, Germany, in late 1996. In the framework of the Remote Sensing of Sea Ice (FEME) Project, he worked on SAR observation of ocean waves in the marginal ice zone. He is now a Research Scientist with the Remote Sensing Technology Institute (IMF), DLR. The main interest of his present work is the use of complex SAR data to derive two-dimensional ocean wave spectra. Apart from that, he is working on the application of cross-track interferometric (InSAR) data to measure sea surface elevation models.

Birgit Schättler received the Diploma degree in mathematics from the Bayerische Julius Maximilians Universität, Würzburg, Germany, in 1986.

She joined the German Remote Sensing Data Center (DFD), German Aerospace Center (DLR), Oberpfaffenhofen, Germany, in 1987, for the development of the German Processing and Archiving Facility for ERS. At this time, she is responsible for ERS SAR product quality control and validation at the German PAF. Together with H. Breit, she designed and implemented the multisensor BSAR system for ERS, Radarsat, and SRTM/X-SAR data processing.

Helko Breit received the Diploma degree in electrical and information engineering from the Technical University of Münich, Münich, Germany, in 1990.

He joined the German Aerospace Center (DLR) in 1990 for the development of X-band SAR processor in the SIR-C/X-SAR Project. Together with B. Schättler, he designed and implemented the multisensor BSAR system for ERS, Radarsat, and SRTM/X-SAR data processing. At this time, he is concerned with the calibration of SRTM/X-SAR InSAR processing system.

Jochen Horstmann received the Diploma degree in physical oceanography from the University of Hamburg, Hamburg, Germany, in 1997.

In 1995, he joined the Coupled Model System Group, GKSS Research Center, Geesthacht, Germany. In the framework of marine parameters from radar images (SARPAK), he worked on extraction of parameters from SAR. Since 2000, he ihas been a Research Scientist working in the ENVOC Project, GKSS Research Center. His research interests are in the extraction of wind fields from SAR. He is also working on algorithms to determine marine parameters from SAR images and application of interferometric SAR.